Supporting Information

Optoelectronic and Spectroscopic Characterization of Vapor-Transport Grown Cu_2ZnSnS_4 Single Crystals

Tat Ming Ng[a,b], Mark T. Weller[b], Gabriela P. Kissling[b], Laurence M. Peter[b,*], Phillip Dale[c], Finn Babbe[c], Jessica de Wild[c], Bernard Wenger[d], Henry J. Snaith[d], David Lane[e]

a. Centre for Sustainable Chemical Technologies, University of Bath, Bath BA2 7AY, UK

b. Department of Chemistry, University of Bath, Bath BA2 7AY, UK

c. Physics and Materials Science Research Unit, University of Luxembourg, 41, rue du Brill, L-4422 Belvaux, Luxembourg

d. University of Oxford, Clarendon Laboratory, Parks Road, Oxford, OX13PU, UK

e. Cranfield Forensic Institute, Cranfield University, Defence Academy of the United Kingdom, Shrivenham, SN6 8LA, UK

*. l.m.peter@bath.ac.uk

Growth of CZTS crystals and Cooling Curve

CZTS was synthesized in evacuated quartz ampules using copper (Sigma Aldrich 99.7%), zinc (Alfa Aeser, 99.9%), tin (Alfa Aeser 99.85%) and sulfur (Alfa Aeser 99.999%). The amounts of material and conditions used in the synthesis of the CZTS precursors for crystal growth were as follows. Needle precursor: Cu 2.3807 g, Zn 1.8368 g, Sn 2.7786 g, S 4.2093 g, 900° C for 2 days. Platelet precursor: Cu 6.2424 g, Zn 4.2829 g, Sn 6.4782 g, S 7.0112g, 750° C for 43 days. The needles were grown using ~10 g CZTS and ~0.2 g I_2 (Sigma Aldrich 99.999%), 8 days. The platelets were grown using 6.033 g CZTS, 0.749 g I_2 and 0.06 g NaI (99+%, Sigma Aldrich), 9 days. The crystals were cooled in situ after switching off the furnace. The cooling curve is shown in Fig. 1.

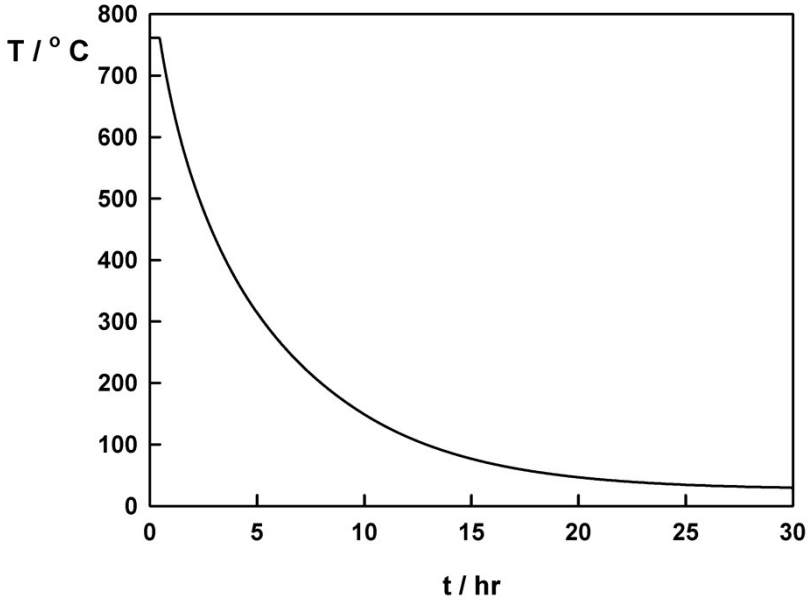

Fig. 1. Measured Cooling curve for Growth Zone of the 4-zone furnace.

Spectroscopic Ellipsometry

The crystals' complex dielectric functions ($\varepsilon = \varepsilon^{'} + i\varepsilon^{''}$) were determined using spectroscopic ellipsometry. The crystals were mounted in epoxy resin and Teflon and polished to 1µm using alumina paste, and optical microscopy was used to select areas for examination. This was done using a J.A. Woollam M20000U-Xe rotating compensator ellipsometer with focusing optics that gave a 150 µm wide spot. Measurements were carried out over a spectral range of 245 to 1690 nm

(0.734 to 5.044 eV) at three angles of incidences (45, 55 and 65°). The resulting data were analysed using the computer program CompleteEASE.[1]. This was done in two stages. First the ellipsometric parameters (Ψ and Δ) were fitted by approximating ε by a B-spline. This allowed arbitrary flexibility whilst enforcing Kramers-Kronig consistency and a positive ε_2 to ensure a physically meaningful solution. ε was then refined by converting the B-spline into a general oscillator model where its main features were represented by PSEMI-M0 oscillators[2,3], and Gaussian peaks were used to improve the overall fit. The absorption coefficient values derived by fitting the spectroscopic ellipsometry data for the platelet sample are compared with published data in Fig. 2.

Fig. 2. Comparison of α values derived by SE for platelet sample with data from Li et al.[4] for reactively sputtered thin films and tabulated by Ito[5] based on SE data from ref [6].

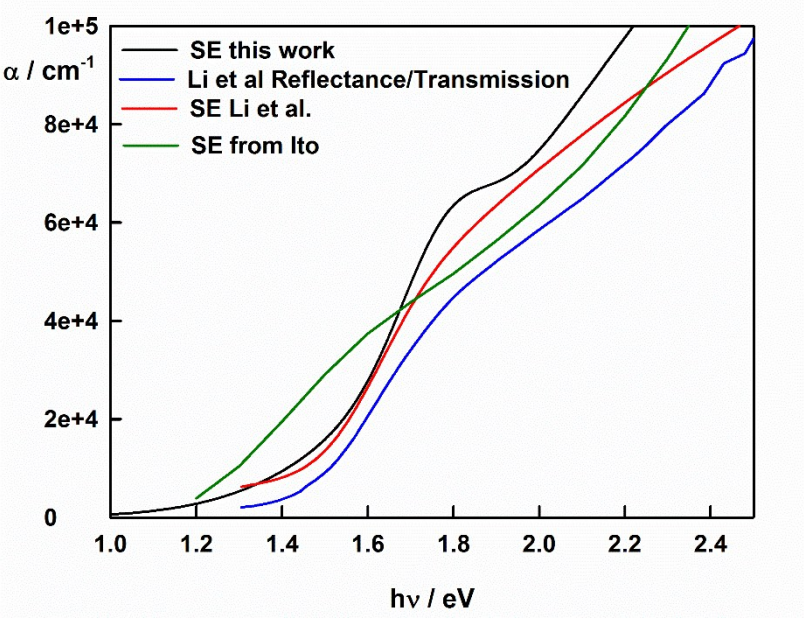

Fig. 3 shows the Tauc plot obtained using the absorption coefficient determined by SE.

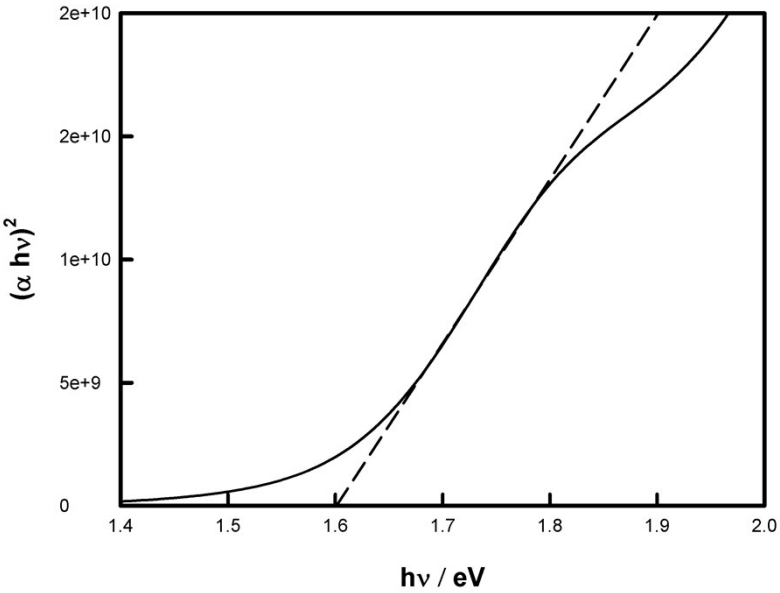

Fig. 3. Tauc plot of absorption coefficient data obtained by spectroscopic ellipsometry (platelet crystal)

Fig. 4 shows the Urbach plot for the SE data.

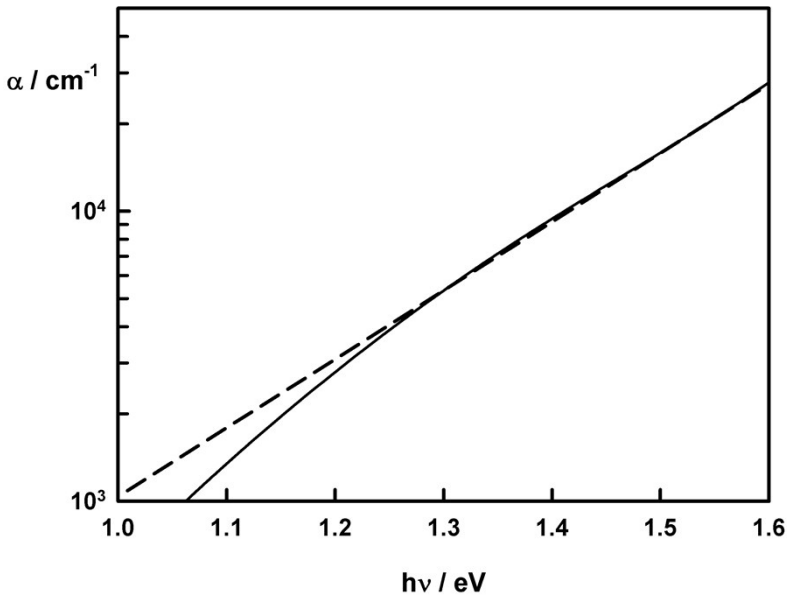

Fig. 4. Urbach plot of absorption coefficient obtained by SE for the platelet crystal.

Photocurrent Spectroscopy

Chopped collimated illumination was provided by a tungsten lamp and grating monochromator (Bentham Instruments) with a variable frequency mechanical chopper operating at 27 Hz, and the photocurrent was detected by a lock-in amplifier (Stanford Research). The spot size of the illumination was controlled by image slits and was chosen to be smaller than the smallest dimension of the crystals to ensure that all the light fell on the crystal surface. The illumination intensity was measured using a calibrated silicon photodiode traceable ±5% to NBS standards. The external quantum efficiency spectra were corrected for reflection losses due to the glass window of the cell and reflection from the crystal surface.

The Tauc plot derived from the EQE data for needle is shown in Fig. 5. The intercept gives a band gap of 1.64 eV, slightly lower than that obtained for the Tauc plot for the platelet (1.68 eV).

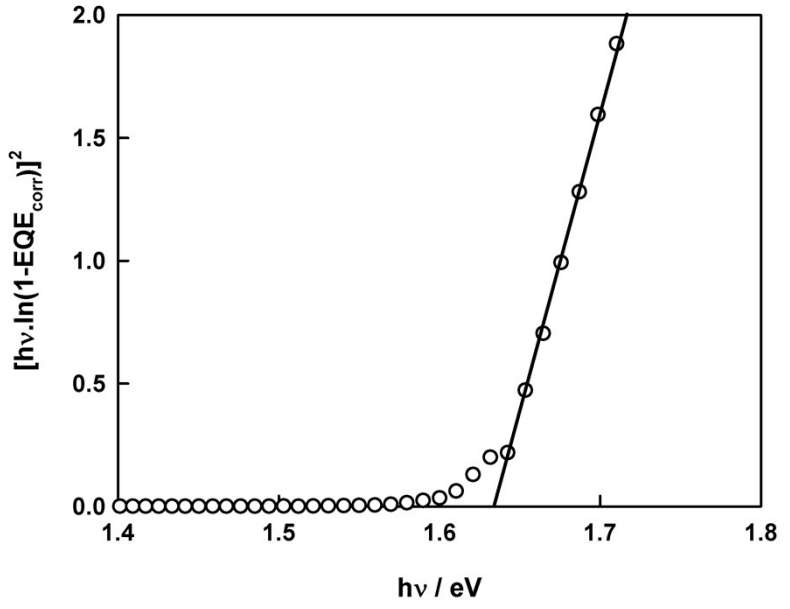

Fig. 5. Tauc plot of the EQE data for the needle sample (E_g = 1.64 eV).

The Urbach plot of the EQE data for the platelet is shown in Fig. 6.

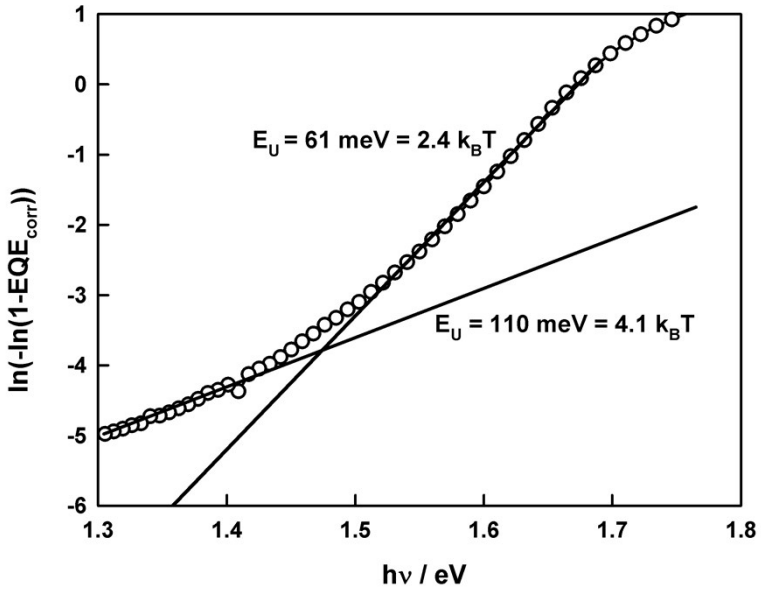

Fig. 6. Urbach plot of EQE data for the platelet.

Electrolyte Electroreflectance

For electrolyte electroreflectance measurements, unchopped illumination was incident on the crystal surface at 45°, and the reflected beam was detected by silicon photodiode. The electrode potential was modulated by an ac voltage of variable frequency and amplitude provided by the lock-in amplifier, which also detected the modulated reflectance signal from the photodiode. EER spectra reported here were recorded using 13 Hz modulation. The validity of the low field approximation was checked by varying the amplitude of the ac modulation. The results shown in Fig. 7 show that the EER signal depends linearly on the amplitude of the ac modulation as expected.

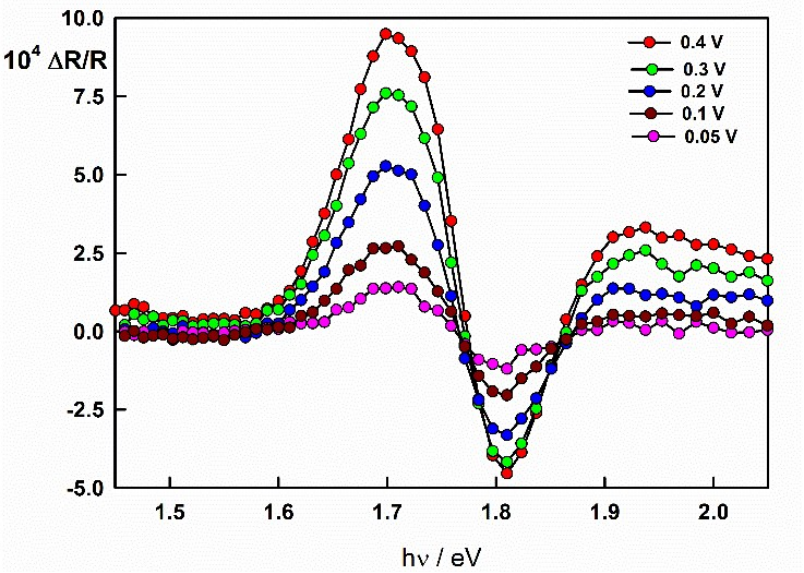

Fig.7. Dependence of the EER signal on modulation amplitude measured for the CZTS platelet sample at -0.6 V vs Ag/AgCl.

Raman Spectroscopy

Fig. 8 shows the fitting of the resonant Raman spectra of the as-grown platelet and needle.

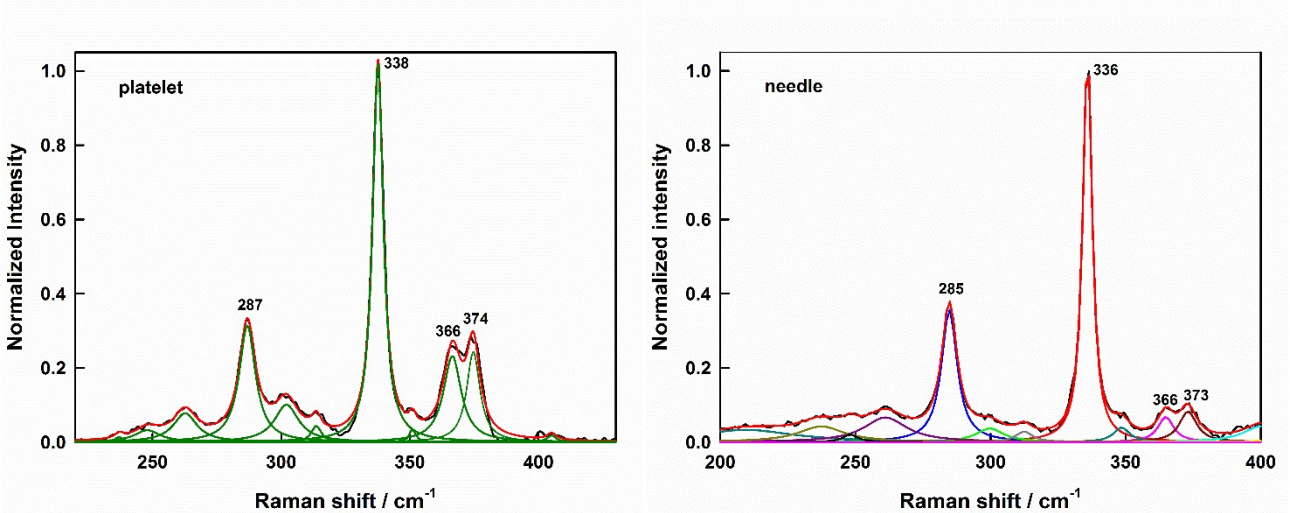

Fig. 8. Deconvolution of near-resonant Raman spectra of the as-grown platelet and needle (red lines total fit).

Assignment of the Raman peaks used to identify the kesterite phase

Platelet			**Needle**			**Theoretical kesterite** [7,8]			**Theoretical stannite** [7,8]		
Modes	Wavenumber (cm^{-1})		Modes	Wavenumber (cm^{-1})		Modes	Wavenumber (cm^{-1})		Modes	Wavenumber (cm^{-1})	
A	338		A	336		A	340.04/335.2		A_1	334.08/332.7	
	302			300			284.30/309.0			277.12/309.1	
	287			285			272.72/302.1		A_2	263.11/304.3	
B (TO LO)	351	375	B (TO LO)	349	373	B (TO LO)	355.80/354.8	374.05/366.4	B_1	291.12/324.1	
							309.56/332.7	313.19/336.1		74.17/88.1	
	236	249		237	250		238.48/269.1	254.73/285.1	B_2 (TO LO)	360.12/358.5	370.63/364.2
							166.65/179.6	168.21/179.9		277.08/306.2	291.82/320.6
							98.82/104.2	98.83/104.3		149.69/171.0	150.91/171.1
							86.70/92.3	87.51/93.1		95.85/96.4	95.86/96.4
E (TO LO)		366	E (TO LO)		365	E (TO LO)	351.55/341.4	366.35/353.2	E (TO LO)	346.01/341.3	364.87/353.7
		314			313		281.07/309.7	293.44/314.1		264.34/305.3	275.52/311.9
	245	263			261		250.26/278.2	257.85/289.8		235.41/268.7	246.58/283.3
							150.53/166.1	151.05/166.2		161.68/170.9	162.63/171.0
							105.93/101.4	106.00/101.4		97.34/106.9	97.38/106.9
							83.64/79.2	83.65/79.2		78.39/74.9	78.73/75.5

Vineyard model

The Vineyard model[9] of order-disorder transformations gives the rate constants .

$$k_{order} = 4f\exp\left(\frac{-U}{k_B T}\right)\exp\left(\frac{3\nu S}{k_B T}\right) \quad k_{disorder} = 4f\exp\left(\frac{-U}{k_B T}\right)\exp\left(\frac{-3\nu S}{k_B T}\right)$$

and the rate of change of order as

$$\frac{dS}{dt} = \frac{1}{2}\left[k_{order}\left(1-S\right)^2 - k_{disorder}\left(1+S\right)^2\right]$$

Here f is the frequency of the vibrational mode involved in the exchange of neighbouring atoms (taken as ~10^{12} Hz), U is the activation energy for place exchange (taken as 14900/k_B) and ν (taken as 358/k_B) is related to the interaction energies of the three possible nearest neighbour pairs (Cu-Cu, Zn-Zn and Cu-Zn). The values of U and ν used in the calculations shown here were taken from the fit obtained by Scragg et al.[10] Equilibrium is established at a given temperature when dS/dt = 0, as illustrated in Fig. 9 for a temperature of 150°C

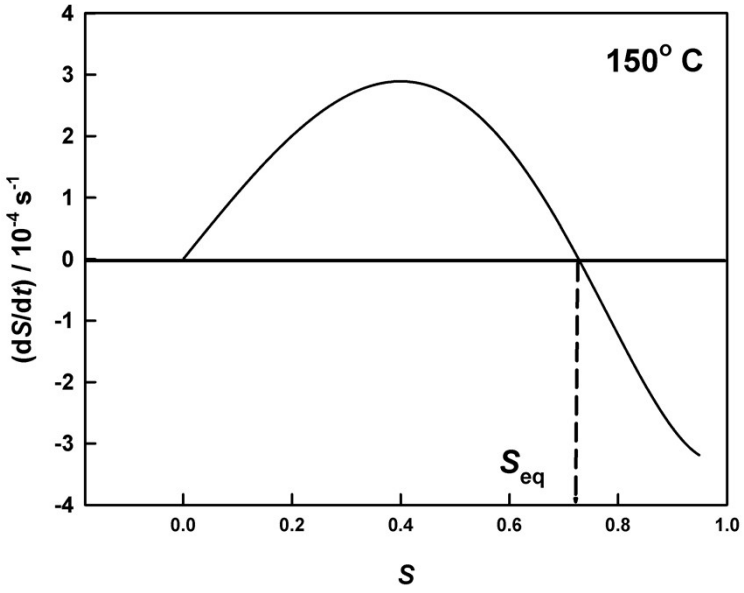

Fig. 9. Plot showing definition of equilibrium order when dS/dt = 0 for T = 150°C.

The predicted time dependence of the order parameter S for a temperature of 100°C is illustrated in Fig. 10.

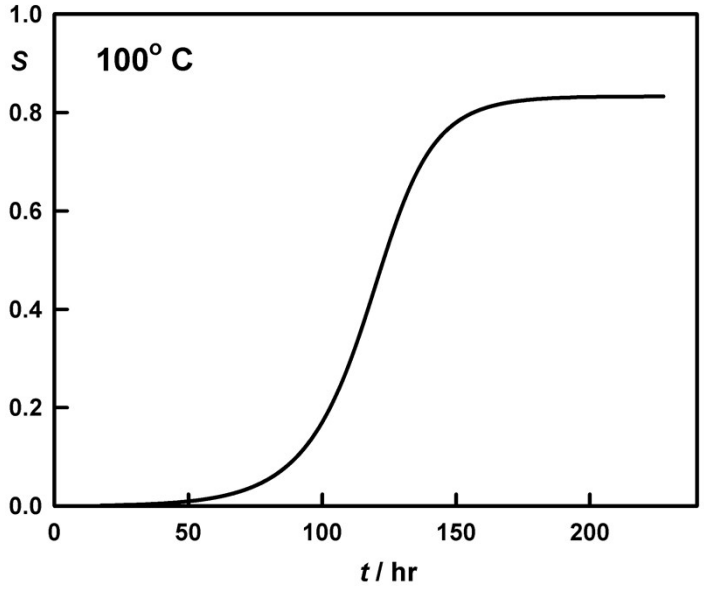

Fig. 10. Time-dependence of the order parameter S predicted for the annealing of a fully disordered crystal at 100°C.

The predicted equilibrium order parameter as a function of annealing temperature is illustrated in Fig. 11.

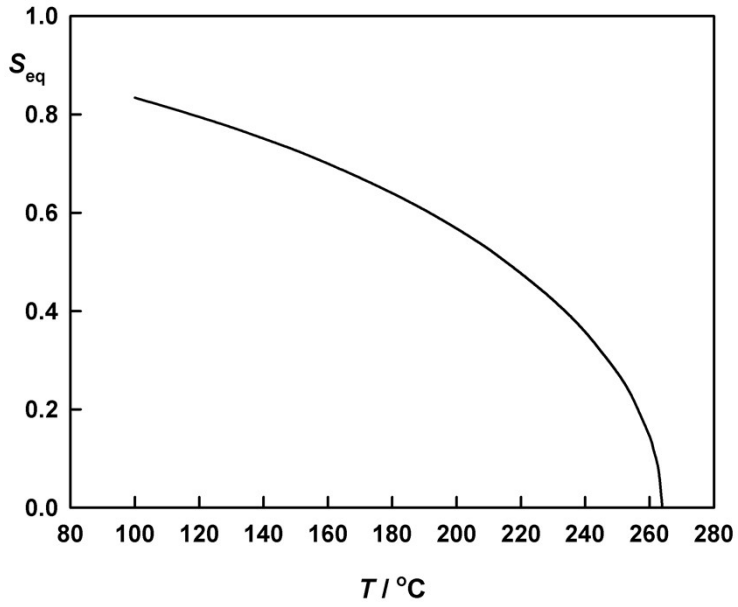

Fig. 11. Equilibrium Order Parameter *S* as a function of annealing temperature calculated from the Vineyard model for values given in text.

Photoluminescence

Photoluminescence spectra were recorded in a homebuilt set up. A green (514 nm) CW argon laser was used with a power of 1 mW and diameter of 100 µm and integrated over several minutes to obtain an optimized signal. The spectra were measured between 550 and 1050 nm with a Si camera and between 900 and 1250 nm with an InGaAs camera. High pass filters of 550 nm for the Si to exclude laser light and 850 nm for the InGaAs to exclude second order light (from laser and the sample) were used.

Time-resolved photoluminescence measurements where performed in air with a photon counting system (Fluotime 300, PicoQuant GmbH). The samples were excited with a 634 nm laser diode (LDH-P-C-635, PicoQuant GmbH, pulse duration 40 ps). Decay traces were acquired at an excitation fluence of 2.3 µJ/cm^2. We used an IR-PMT detector (Hamamatsu, H12694) to measure decays at 1.30 eV and a PicoQuant PMA-Hybrid detector for decays at 1.65 eV.

Fig. 12 compares the blue shift measured for the platelet and needle samples

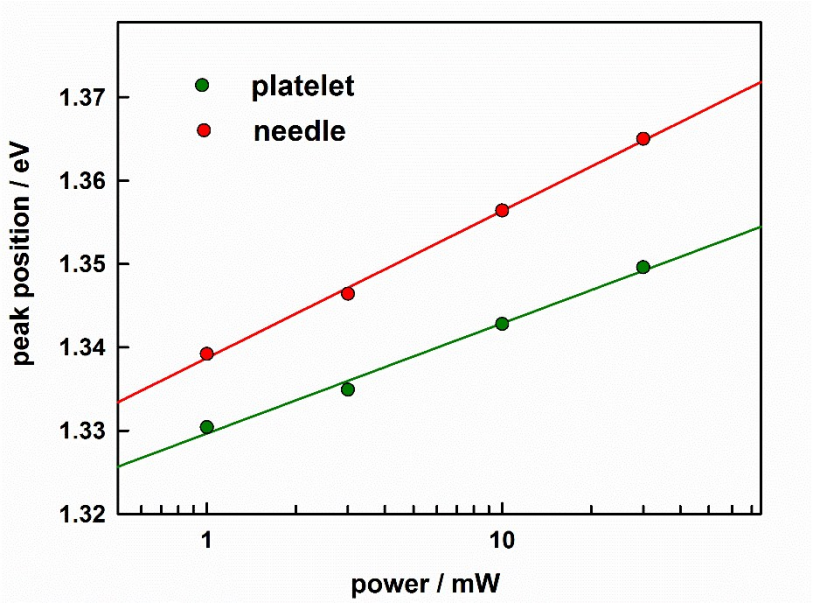

Fig. 12. Intensity dependence of PL peak energy for platelet and needles crystals

Fig. 13 shows the dependence of PL intensity on laser power for the platelet and needle samples.

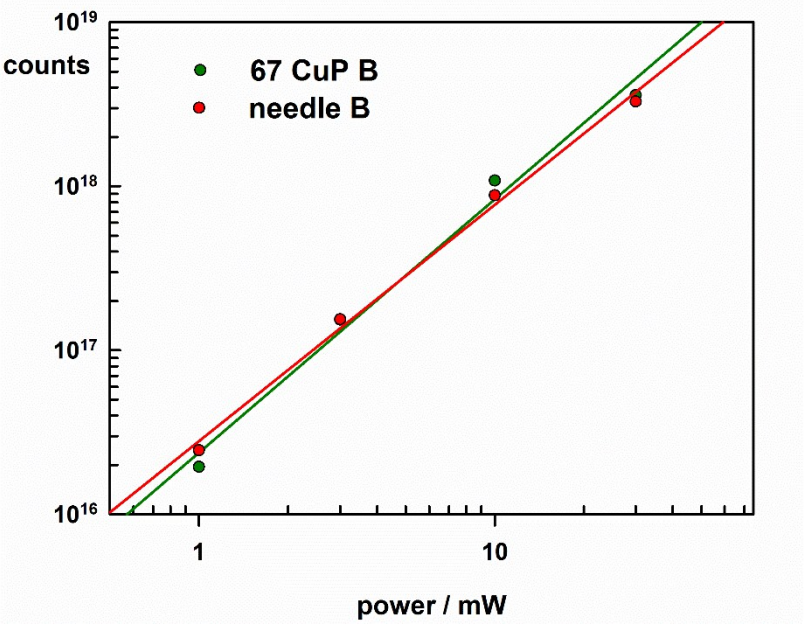

Fig. 13. Dependence of PL intensity on laser power for platelet and needle crystals.

Fig. 14 shows the PL decays measured at two different photon energies in the case of the CZTS needle. The decay times are almost identical. This contrasts with the energy dependence of the lifetime the platelet sample shown in the main text.

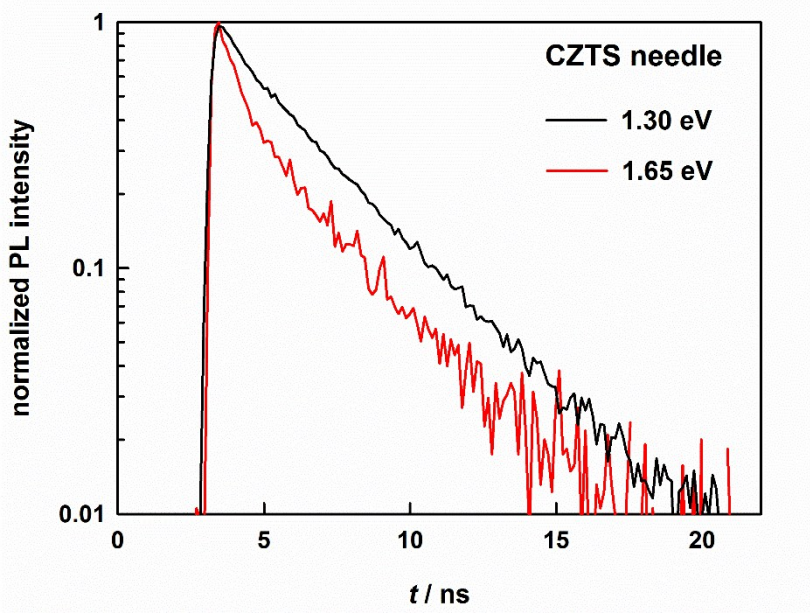

Fig. 14. PL decay plots for the CZTS needle at two different emission energies. Excitation energy 1.96 eV

Attempt to obtain the electron diffusion length using Gärtner analysis

Close to the bandgap, where αL_n<<1, the Gärtner equation

$$EQE = 1 - \frac{\exp -\alpha W}{1 + \alpha L_n}$$

reduces to the simpler form

$$-\ln(1 - EQE) = \alpha W$$

If the semiconductor/electrolyte interface behaves ideally (no surface states), the width of the space charge region should vary with the square root of $U_{fb} - U$, where U_{fb} is the flat band potential.

$$W_{SC} = \left(\frac{2\Delta(U_{fb} - U)\varepsilon\varepsilon_0}{qN} \right)^{1/2}$$

It follows that a plot of $[\ln(1 - EQE)]^2$ vs. electrode potential U should have an intercept at U_{fb}. Fig. 15 shows plots for two wavelengths close to the band edge, from which the flat bad potential is estimated to be -0.5 V vs Ag/AgCl.

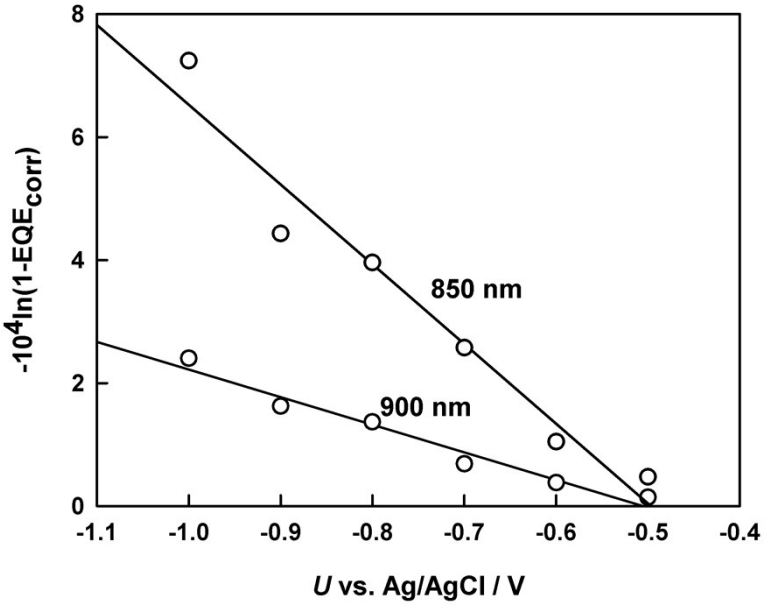

Fig. 15. Plots used to estimate the flat band potential of CZTS

The Gärtner equation can also be written in the form

$$-\left[\ln(1 - EQE) + \ln(1 + \alpha L_n)\right] = \alpha W = \alpha \left(\frac{2\Delta(U_{fb} - U)\varepsilon\varepsilon_0}{qN} \right)^{1/2}$$

so that a plot of -ln(1-EQE) vs. $(U_{fb} - U)^{1/2}$ should have an intercept on y axis equal to ln(1+ αL_n). Fig. 16 shows plots of this function for three different wavelengths. The plots are clearly non-linear and so it is not possible to obtain a reliable value of the intercept on the y axis. We attribute this to non-ideal behaviour of the CZTS/electrolyte junction due to the presence of a high density of surface states. The charging of these surface states leads to a change in the potential drop across the Helmholtz layer when the electrode potential is altered, so that the simple square root relationship between the width of the space charge region and (U_{fb}-U) no longer holds.

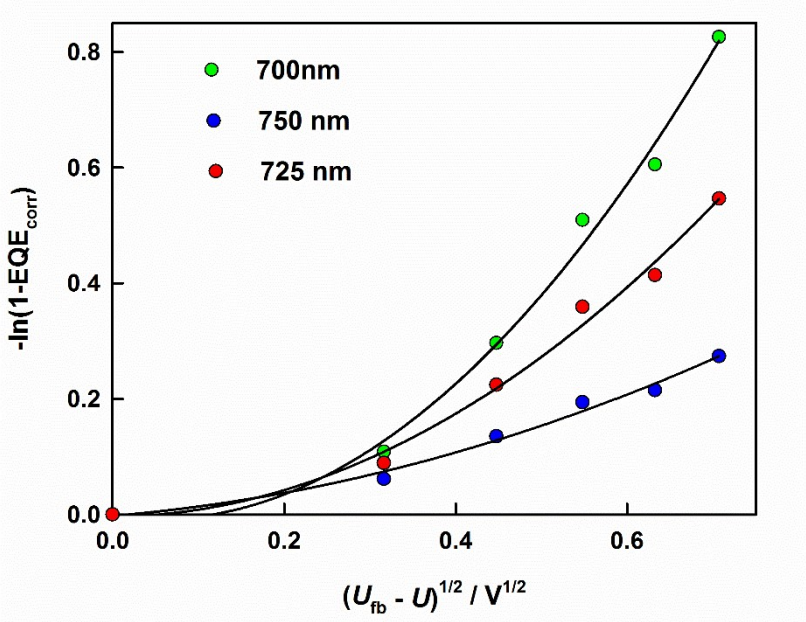

Fig. 16. Plots of -ln(1-EQE) vs .(U_{fb}-U) according to the Gärtner equation showing non-ideal junction behaviour

Impedance Measurements

Impedance measurements were carried out using a Solartron Modulab system and fitted using ZView software (Scribner). The impedance behaviour of the platelet crystal shows that the evaporated Au contact is non-ohmic with a series resistance greater than 1 kΩ and a stray capitance of around 800 pF. The series resistance is not a problem for the very low currents and low chopping frequencies in the EQE measurements.

An example of the impedance fitting to the equivalent circuit on the next page is shown below for data measured at -1.0 V vs. Ag/AgCl. The low frequency behaviour is consistent with the presence of a high surface state capacitance, modelled here by the constant phase shift element CPE1. Reliable fitting and extraction of the space charge capacitance proved difficult due to the overlap in time constants for the surface state and space charge capacitances, and consequently construction of Mott-Schottky plots to determine the doping density of the crystal was not possible.

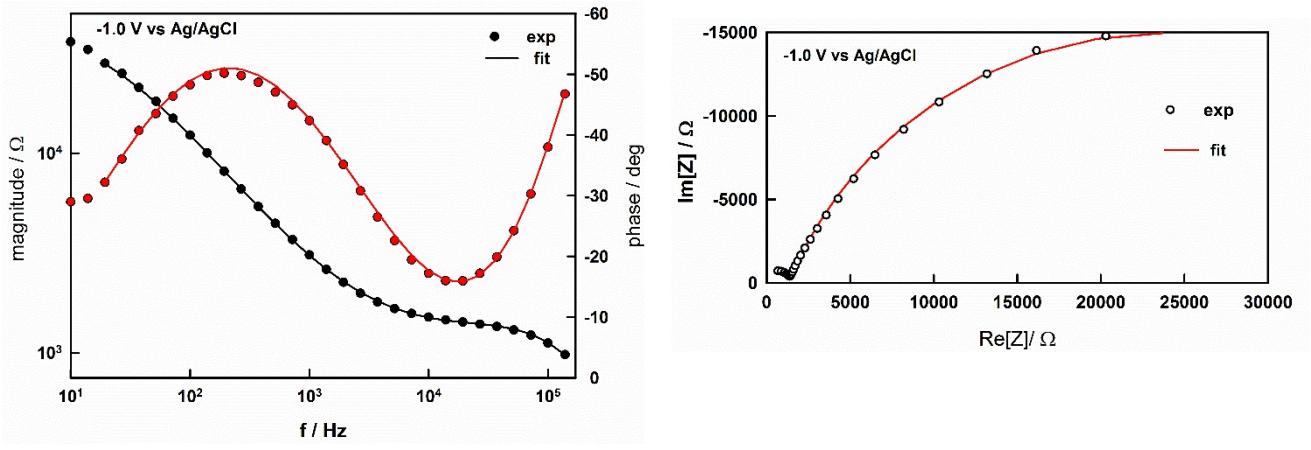

Fig. 17. Bode and Nyquist plots of impedance of etched CZTS platelet crystal. The fitting data are given below.

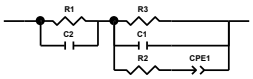

Element	Freedom	Value	Error	Error %
R1	Free(+)	1376	6.4889	0.47158
C2	Free(+)	8.6322E-10	7.3385E-12	0.85013
R3	Free(+)	46185	1034.5	2.2399
C1	Free(+)	4.1256E-08	1.2771E-09	3.0955
R2	Free(+)	1537	201.27	13.095
CPE1-T	Free(+)	7.2261E-07	4.1279E-08	5.7125
CPE1-P	Free(+)	0.67597	0.0078146	1.1561

Chi-Squared:	0.00021708
Weighted Sum of Squares:	0.010637
Data File:	C:\Users\chsImp\LMP Files\Papers 2016\CZTS single crystal\SI Figures\impedance at -1 V.txt
Circuit Model File:	
Mode:	Run Fitting / Selected Points (0 - 27)
Maximum Iterations:	100
Optimization Iterations:	0
Type of Fitting:	Complex
Type of Weighting:	Calc-Modulus

R_1 contact resistance

R_2 surface state resistance

R_3 Faradaic resistance

C_1 space charge capacitance

C_2 contact capacitance

CPE1 surface state CPE

References

1. J. A. Woollam Co. Inc., Lincoln, NE, US

2. US Patent 5,796,983, “Dielectric function parametric model, and method of use”, 18 August 1998, C. M. Herzinger, B. D. Johs, J. A. Woollam Co. Inc., Lincoln, NE, US

3. B. Johs, C.M. Herzinger, J.H. Dinan, A. Cornfeld, J.D. Benson, *Thin Solid Films*, 1998 1**37-142**, 313-314

4. S-Y Li, C. Hägglund, Y Ren, J.J.S. Scragg, J.LK. Larsen,C. Frisk,K. Rudisch,S. Englund, C. Platzer-Björkman, *Solar Energy Materials and Solar Cells* 2016**, 149**, 170-178.

5. K. Ito, *Copper Zin Tin Sulfide-based Thin Film Solar Cells*. Wiley: Chichester, United Kingdom, 2015; p 421.

6. J. Li, H.Du, J. Yarbrough, A. Norman, K. Jones, G. Teeter, F.L. Terry, D. Levi, *Optics Express* 2012**, 20**, (S2), A327-A332.

7. T. Gurel, C. Sevik and T. Cagin, *Physical Review B*, 2011, **84**. 205201.

8. A. Khare, B. Himmetoglu, M. Johnson, D. J. Norris, M. Cococcioni and E. S. Aydil, *J. Appl. Phys.*, 2012, **111**, 083707.

9. G. Vineyard, Phys. Rev. 1956, **102**, 981.

10. J.J.S. Scragg, J. K. Larsen, M. Kumar, C. Persson, J. Sendler,S. Siebentritt, C.P. Bjorkman, *Physica Status Solidi B-Basic Solid State Physics* 2016**, 253**, (2), 247-254.